
This manuscript is a preprint and will be shortly submitted for publication to a scientific journal. As a function of the peer-reviewing process that this manuscript will undergo, its structure and content may change.

If accepted, the final version of this manuscript will be available via the 'Peer-reviewed Publication DOI' link on the right-hand side of this webpage. Please feel free to contact any of the authors; we welcome feedback.

A breakthrough in fast flood simulation

B. van den Bout^{1*}, V. G. Jetten¹, C. J. van Westen¹, L. Lombardo¹

¹ *University of Twente, Faculty of Geo-Information Science and Earth Observation*

[*b.vandenbout@utwente.nl](mailto:b.vandenbout@utwente.nl)

Twente University,

Hengelosestraat 99, 7514AE, Enschede, The Netherlands

Highlights

- *A new innovative fast approximate flood simulation method*

- *Employment of fast sweeping numerical algorithms to quickly estimate flow networks*

- *Over 1500 times faster in the shown cases of flash and fluvial floods, with similar accuracy to full simulation*

Abstract

The current status of technological advancement does not allow to generate complete flood simulations in real-time for large geographic areas. This hinders warning-systems, interactive planning tools and detailed forecasts and as a consequence the population cannot be quickly or reliably informed of where large masses of water will flow. Our novel method computes flood hazard maps over three orders of magnitude faster than current state-of-the-art methods. It applies physically-based principles of steady-state flow to evade full dynamic aspects of flood simulations. It directly estimates the relevant information for flood hazard, such as peak flow height, velocity and flood arrival time. Performance indicators show similar or exceeding accuracy compared to traditional flow models depending on the type of event and quality of the used elevation data. In our tests, computational costs are reduced on average by a factor 1500. As a result, the developed method provides new perspective for the field of flood hazards, flood risk reduction through new types of early-warning systems, and user-interactive hazard assessment systems. As climate change is expected to aggravate flood hazard, the presented method can bring necessary efficiency to flood simulation and thereby save lives and livelihoods.

Keywords: Floods, Flow networks, Algorithms, Forecasting.

1. Introduction

Floods are the most frequently occurring type of disasters, and 44% percent of all disasters occurring in the past decades consists of coastal, alluvial, flash floods and pluvial floods (UNDRR, 2020). The immense world-wide economic and social impacts of flooding urge for more efforts in flood risk reduction, where fast and accurate flood hazard assessment tools play a crucial role (Stelling & Verwey, 2006). Physically-based numerical simulation tools have been applied to Disaster Risk Reduction (DRR) and Early Warning Systems (EWS) in both national scale and local scale. Such models generally employ an adaptation of the Saint-Venant equations for shallow water flow, combined with force descriptions related to gravity, pressure and friction (Delestre et al., 2014). When parameterized with elevation, surface and sub-surface related data, a full dynamic simulation is carried out. These models provide relevant information such as maximum flow height, maximum flow velocity and flood arrival time (Sanders, 2017).

The applicability of physically-based flood modelling has suffered from its computational demands. Efficient, simplified methods (e.g. non-spatial: curve-number method or the rational method) remained popular in engineering applications (Rahman, Haddad, Zaman, Kuczera, & Weinmann, 2011). These tools predict only peak discharge, and are much less dependent on data quality and spatial details. Heuristic approaches exist in the form of fast approximate cellular automata (Gibson

44 et al., 2016; Jamali, Bach, Cunningham, & Deletic, 2019) and machine learning models (Mosavi,
45 Ozturk, & Chau, 2018). These computational systems lose their physical basis but can be designed to
46 quickly replicate the flowing behavior of water. Full spatial dynamical simulations have also seen
47 improvements to efficiency. Techniques such as quad-tree domain subdivision, supercell water
48 redistribution and parallelization on CPU and GPU compute power have been adopted for a
49 significant reduction in computation times (Kalyanapu, Shankar, Pardyjak, Judi, & Burian, 2011; Liang,
50 Du, Hall, & Borthwick, 2008; Yu & Lane, 2006). However, despite the benefits of all these techniques,
51 current method remain either too inaccurate for flood hazard assessment, or too computationally
52 demanding for real-time application.

53 In this article, we present a new method for computation of flood hazard maps that decreases
54 simulation time by a factor 1514 on our five study sites. Our method (SFFS; Super-Fast Flood
55 Simulation) is based on the Steady-State assumption, which entails the incoming and outgoing
56 discharge (q) in each area are equal, resulting in zero net height change over time. Steady state
57 conditions are not commonly met in nature, as rainfall and infiltration are dynamic processes.
58 However, we apply an innovative approach to employ steady state simulation in order to speed up
59 regular flood hazard simulation. In section two, we describe the method and related algorithms. In
60 section three, we compare the method with full simulation, observations and other fast approximate
61 methods for various type of flood events. In section 4 we discuss the potential usage, strengths and
62 benefits of the new method.

63 2. Materials and methods

64 The method uses a combination of four innovative concepts, which are further expanded in the
65 methods section.

- 66 • Fast steady-state flow accumulation solver
- 67 • Inversion of flow accumulation field
- 68 • Compensation for partial steady-state (when applicable)
- 69 • Adaptive solver to refine pressure-driven inundation

70 The data requirements for the method are limited compared to more advanced flood simulation
71 models. Our models requires data on the event duration, and rainfall intensity (can be spatial),
72 Mannings Surface roughness (can be spatial) and elevation of the terrain. These datasets can be
73 obtained from global datasets of rainfall (e.g. GPM), elevation (e.g. SRTM), and land cover (e.g.
74 Corine, GlobCover), which gives the opportunity to use the model in data scarce regions. More
75 detailed datasets (e.g. LiDAR-based elevation data) and field measurements and verification,
76 however, are critical in obtaining high quality data. Note that, because of the steady-state
77 assumption, the model is not fully dynamic. The presented method attempts to circumvent the need
78 for full dynamic simulation, instead directly estimating several variables that are of high importance.
79 Outputs include peak flow height, peak flow velocity, peak discharge and flood arrival time.

80 2.1 Steady State Flow Accumulation

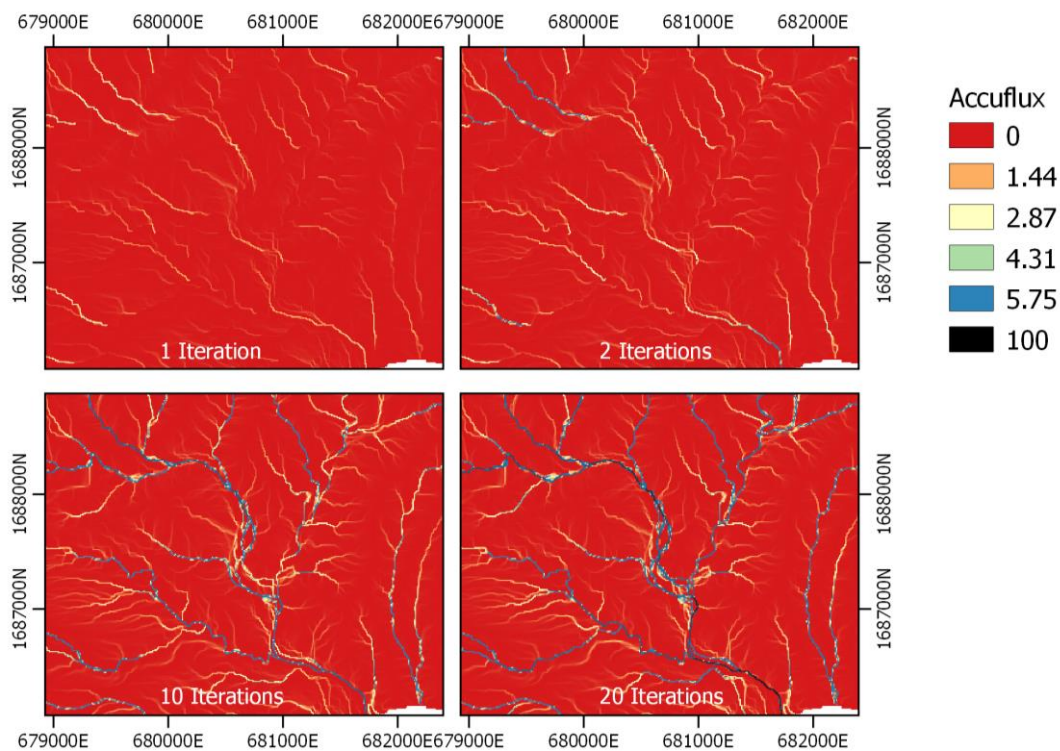
81 The steady-state solver is based on flow theory, which is closely linked to the Saint-Venant equations
82 and considers flow states with time-constant input, and a resulting non-dynamic flow states (de
83 Saint-Venant, 1871). In such cases, a constant velocity field is present, and mass conservation results
84 in inflow equal to outflow ($Q_{in} = Q_{out}$, where Q is water discharge). A special property of these flow
85 states is that accumulation of water sources through the network is equal to the steady-state
86 discharge, as the accumulation of all upstream incoming flows must equal local outflow.

87 We developed an extremely efficient algorithm for steady-state flow using multi-directional
 88 sweeping, based on the fast sweeping method (Zhao, 2005). Traditional methods loop over elements
 89 of the domain and transfer fluxes to direct neighbors. Our implementation sweeps the data through
 90 the velocity-field in-place, allowing for material to travel large stretched of space in a single
 91 iterations. In particular, as long as the principle directions are the same, the material flux can be
 92 accumulated through the network within a single iteration. For more general application, material
 93 moves along similar directions in a single iteration (Figure 1).



94
 95 *Figure 11 Left) Traditional flow accumulation algorithm. Right) Our implementation using multi-directional sweeping.*

96 As a result, typical flow accumulation over terrain is solved an order of magnitude faster. In the
 97 example of figure 2, only requiring 21 iterations as opposed to 820, while the terrain is far from a
 98 smooth ideal case.



99
 100 *Figure 2 The accumulation of flow after several iterations of our multi-directional sweeping algorithm. Area is the Grand-Bay*
 101 *catchment on Dominica.*

102 We use this algorithm first to create a monotonically-increasing elevation model (hydrologically-
103 corrected). Using the same multi-directional sweep algorithm, we can accumulate direction-specific
104 slope to reconstruct the elevation model. By limiting the slope in x- and y direction to be strictly
105 positive, we can efficiently reconstruct the elevation model without depressions.

106 Using the x- and y-direction gradient of the corrected elevation model as velocity field, we can now
107 accumulate precipitation through the network to get flow accumulation (which equals steady-state
108 flow). Our usage of terrain slope as a directional flow network means that, for now, we ignore
109 pressure forces but only consider gravitational and frictional forces for the direction of movement.
110 This will be compensated in a later stage.

111 2.2 Inversed flow accumulation

112 As a result of the steady-state simulation described above, we have obtained the steady-state
113 discharge in space. Natural systems however, encounter dynamic precipitation, and are often too
114 large to be covered by an approximate steady-state flow. Instead, a discharge wave will propagate
115 through the flow network. We can define the flow accumulation as (Equation 1).

$$116 \quad AF(R) = Q_{af} \quad 1$$

117 Where $AF(x)$ is the flow accumulation algorithm, which takes a source material as input, and returns
118 the accumulated throughput of that source material when it follows the velocity-field.

119 To invert the flow accumulation values and obtain flow heights, we employ Mannings surface flow
120 law, which is an inversion of the momentum balance of kinematic flow. Thus, our flow height
121 becomes (Equation 2).

$$122 \quad h_{af} = \left(\frac{q_{af} n}{dx \sqrt{s}} \right)^{\frac{3}{5}} \quad 2$$

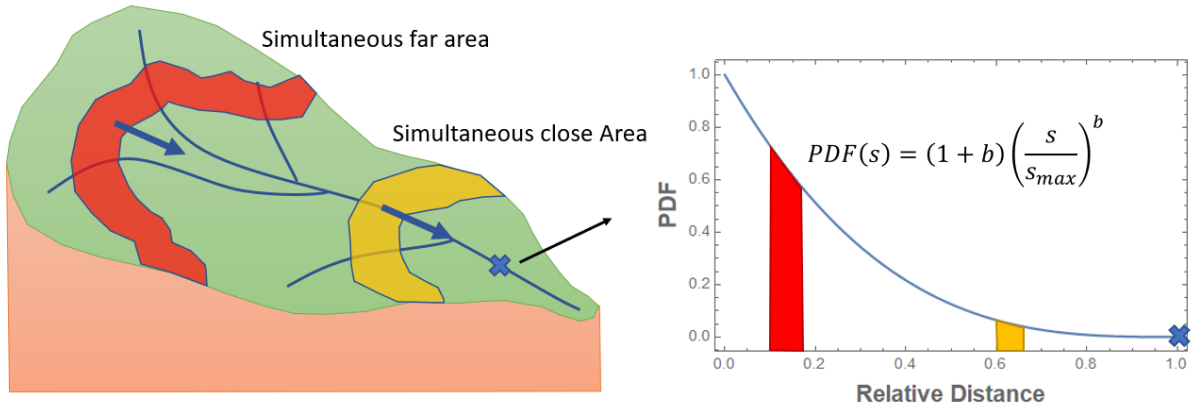
123 The methods described above are the principal components responsible for the speed of the
124 presented method. The fast estimation of steady-state velocity-fields linked with inverted flow
125 accumulation-fields provides an extremely fast method for estimation of steady-state flow heights.
126 Spatial precipitation can be used as input, as the flow accumulation algorithm will then estimate the
127 steady-state flow accordingly.

128 2.3 Compensation for partial steady state

129 In order to compensate for the partial steady-state, we carry out a compensation scheme based on
130 spatial properties of flow networks. When observing the shapes of catchments, it has been often
131 noted that there is a power-type relationship between the distance to an outlet and the contributing
132 area at that distance (e.g. a circle with an outlet at its center has more area further away from the
133 outlet, growing quadratically with distance) (Equation 3).

$$134 \quad PDF(s) = \frac{(1-b)}{s_{max}} \left(\frac{s}{s_{max}} \right)^b \quad 31$$

135 Where PDF is the probability density (normalized), s is the distance (meters), s_{max} is the maximum
136 distance (meters) and b is the catchment shape parameter (-).



137

138
139

Figure 2 There is a direct proportionality between the discharge progression in the flow accumulation scheme and the frequency of pixels with a relative time to arrival for the observation point.

140
141
142
143

From our flow accumulation algorithm, we can define two conditions which let us determine the values of the catchment shape parameter, and the catchment maximum distance. The first condition is the average distance from the gridcells in the catchment to the outlet, which can be obtained through integration of the PDF, or through the flow accumulation method (Equation 4).

$$\langle s \rangle = \frac{\int_0^{s_{max}} s \frac{(1-b) \left(\frac{s}{s_{max}}\right)^b ds}{\int_0^{s_{max}} \frac{(1-b) \left(\frac{s}{s_{max}}\right)^b ds}} = \frac{(1+b) s_{max}}{2+b}, \quad \langle s \rangle = \frac{\Delta x AF(AF(1))}{AF(1)} \quad 4$$

145
146
147
148

The second condition comes from the fact that our methods assume there is a single outlet gridcell, which has specified area. This is the only area that lies between a distance of 0 and Δx . To obtain gridcell density, we scale the PDF with the total number of gridcells ($AF(1)$) and integrate from a distance of 0 to Δx (Equation 5).

$$1 = \int_0^{\Delta x} AF(1) \frac{(1-b) \left(\frac{s}{s_{max}}\right)^b ds}{s_{max}} = AF(1) \left(\frac{\Delta x}{L}\right)^{1+b} \quad 5$$

150
151
152
153

The peak flow of each location depends on the partial steady state of all contributing locations. Thus, we need to know the relative frequencies of probability density function (PDF) of the upstream pixels with respect to normalized simulation time. Some properties of the flow accumulation scheme can be leveraged for this purpose (Figure 6).

154
155
156
157
158
159

Consider now the discharge progressing through the catchment at distance s . Each infinitesimal interval of s represents a set of points within the catchment that are an equal distance removed from the point under consideration. We can express the total discharge currently passing through that set of points as equation 6. The total discharge in an infinitesimal interval (Q_t) is equal to the average unit discharge at that interval ($Q_{unit,t}$) multiplied by the flow width ($\propto PDF(t)$). This assumes a linear kinematic-wave system.

$$Q_t(t) = PDF(t) Q_{unit,t}(t) = \frac{PDF(t) Q_{total}}{PDF(t)} = Q_{total} \quad 6$$

161
162

Where Q_t is the cumulative discharge in an interval of relative time and $Q_{unit,t}$ is the discharge per unit flow width along a relative-time interval of the catchment.

163
164
165

In a rainfall-fed context, areas upstream are fed by a smaller area, so their discharge should be lowered based on the relative size of the area attributing to flow at that point. This assumes precipitation is distributed homogeneously through a catchment.

$$166 \quad \frac{Q_t(s)}{Q_{total}} = \frac{1 - CDF(s_{max} - s)}{CDF(s_{max})} \frac{Q_{total}}{Q_{total}} = \frac{1 - CDF(s_{max} - s)}{1} = 1 - \left(1 - \frac{s}{s_{max}}\right)^{1+b} \quad 7$$

167 Now, we can employ the fact that because of the partial steady-state, each pixel is not fed by its
 168 entire catchment, but instead by an area $1 - CDF(s) - \left(1 - CDF\left(1 - (s - s_{steady})\right)\right)$. Thus, the
 169 non-steady state discharge becomes

$$170 \quad \frac{Q_t(s)}{Q_{total}} = 1 - CDF(s_{max} - s) - \left(1 - CDF(s_{max} - s_{steady})\right) \quad t > t_{event} \quad 8$$

$$171 \quad \frac{Q_t(s)}{Q_{total}} = 1 - CDF(s_{max} - s) \quad t \leq t_{event} \quad 9$$

172 The maximum discharge slice now becomes a matter of taking the peak of this relationship to
 173 compensate the steady-state discharge, which finally becomes

$$174 \quad f_{ss} = 1 - \left(1 - \frac{s}{s_{max}}\right)^{1+b} - \left(1 - \left(1 - \frac{s_{steady}}{s_{max}}\right)^{1+b}\right) \quad s_{max} > s_{steady} \quad 10$$

$$175 \quad f_{ss} = 1 \quad s_{max} \leq s_{steady} \quad 11$$

176 Where f_{ss} is the correction factor that compensates for the partial steady-state flow. Finally, our
 177 corrected peak discharge becomes

$$178 \quad q = AF(R(\Delta x)^2) \quad 12$$

179 2.4 Adaptive Solver to refine pressure-driven inundation

180 Our final step uses a diffusive wave solver that includes gravity, friction, pressure and advection, but
 181 ignored inertial terms. Utilizing a Darcy-Weisbach friction law and linearized gravity term, the
 182 following equations describe the momentum balance (Te Chow, Maidment, & Mays, 1962) (Equation
 183 13 & 14).

$$184 \quad \frac{\partial u_x}{\partial t} \Big|_{steady\ state} = 0 = g \frac{dz}{dx} + g \frac{d\left(\frac{1}{2}h^2\right)}{dx} - g n \frac{u_x |\bar{u}|}{h^{\frac{2}{3}}} \quad 33$$

$$185 \quad \frac{\partial u_y}{\partial t} \Big|_{steady\ state} = 0 = g \frac{dz}{dx} + g \frac{d\left(\frac{1}{2}h^2\right)}{dx} - g n \frac{u_y |\bar{u}|}{h^{\frac{2}{3}}} \quad 14$$

186 Where u is the velocity ($m\ s^{-1}$), z is the elevation of the terrain (m), h is the flow height (m), g is the
 187 gravitational acceleration ($m\ s^{-2}$), and n is Manning's Surface roughness coefficient ($s\ m^{-\frac{1}{3}}$). These
 188 equations lack the inertial part of the Saint-Venant equations. Such simplifications have been
 189 defended extensively in theoretical and modelling work using kinematic and diffusive wave equations
 190 in the literature (Miller, 1984). As a result of the missing terms, they can be solved analytically for the
 191 velocity u , when the elevation and water height fields are known (Equation 15).

$$192 \quad u_x = \sqrt{\frac{3}{n} \left(-\frac{dz}{dx} - \frac{d\left(\frac{1}{2}h^2\right)}{dx} \right)} \quad u_y = \sqrt{\frac{3}{n} \left(-\frac{dz}{dx} - \frac{d\left(\frac{1}{2}h^2\right)}{dx} \right)} \quad 15$$

193 Finally, a mass conservation equation can be applied to the flow heights. Iteratively updating flow
 194 height will finally reach a steady state, as increased water heights increase outflow and the flow
 195 heights converge to an equilibrium (Equation 16).

$$196 \quad h_{i+1} = h_i + dt \left(\frac{d(h_i u_x)}{dx} + \frac{d(h_i u_y)}{dy} + \max(0, R - I) \right) \quad 16$$

197 We apply these equations to the inverted flow height coming from the flow accumulation
 198 compensated for a partial steady-state. However, equation 10 shows that the assumed relationship

199 between flow height and discharge is non-linear, and flow heights in this steady-state are not
200 conserved, while discharges are. For this reason, we adapt equation 16 to flow according to diffusive
201 wave principles, but conserve discharge instead. Finally, we apply this equation instead (Equation
202 17).

$$203 \quad (h_{i+1})^{\frac{5}{3}} = (h_i)^{\frac{5}{3}} + dt \left(\frac{d((h_i)^{\frac{5}{3}} u_x)}{dx} + \frac{d((h_i)^{\frac{5}{3}} u_y)}{dy} + \max(0, R - I) \right) \quad 17$$

204 In order to improve computational speed, we employ a numerical scheme with gradually decreasing
205 artificial velocity. That is, in case of small flow velocities in some locations, and high velocities in
206 others, the global timestep must be small, resulting in many required steps to advect the material
207 through the model domain. In the case of steady-state modelling, we can adapt our model to instead
208 initially have a fixed ratio between flux and the water volume within a gridcell. During the simulation,
209 this constant fraction is linearly altered to become the actual fraction. This helps move large volumes
210 of water initially while maintaining accuracy in the final iterations.

211 2.5 Method summary

212 Thus, our final approach contains the following steps: i) run a minimal steady-state solver to find a
213 stable directional velocity field and carry out flow accumulation on the velocity field to efficiently
214 solve for steady-state discharge, ii) invert discharge to estimate steady-state flow height, iii) run a
215 compensation scheme for the partial steady-state flow of the event. iv) Compensate for pressure-
216 based inundation through an adaptive diffusive-wave solver. Additional features such as reservoirs
217 and channels with confined 1D flow can be implemented with relative ease by adapting the flow
218 accumulation algorithm.

219 2.6 Rainfall Selection

220 The steady-state algorithm requires, for each location, a single precipitation rate to function. Rainfall
221 intensities might fluctuate, and lower precipitation might have a much longer duration compared to
222 higher-intensities. In order to best represent an event, the duration t and intensity R might be
223 chosen to maximize the product $R_{tot} = t R$ within the constraints of the temporal record.

224 2.7 Study Sites and Events

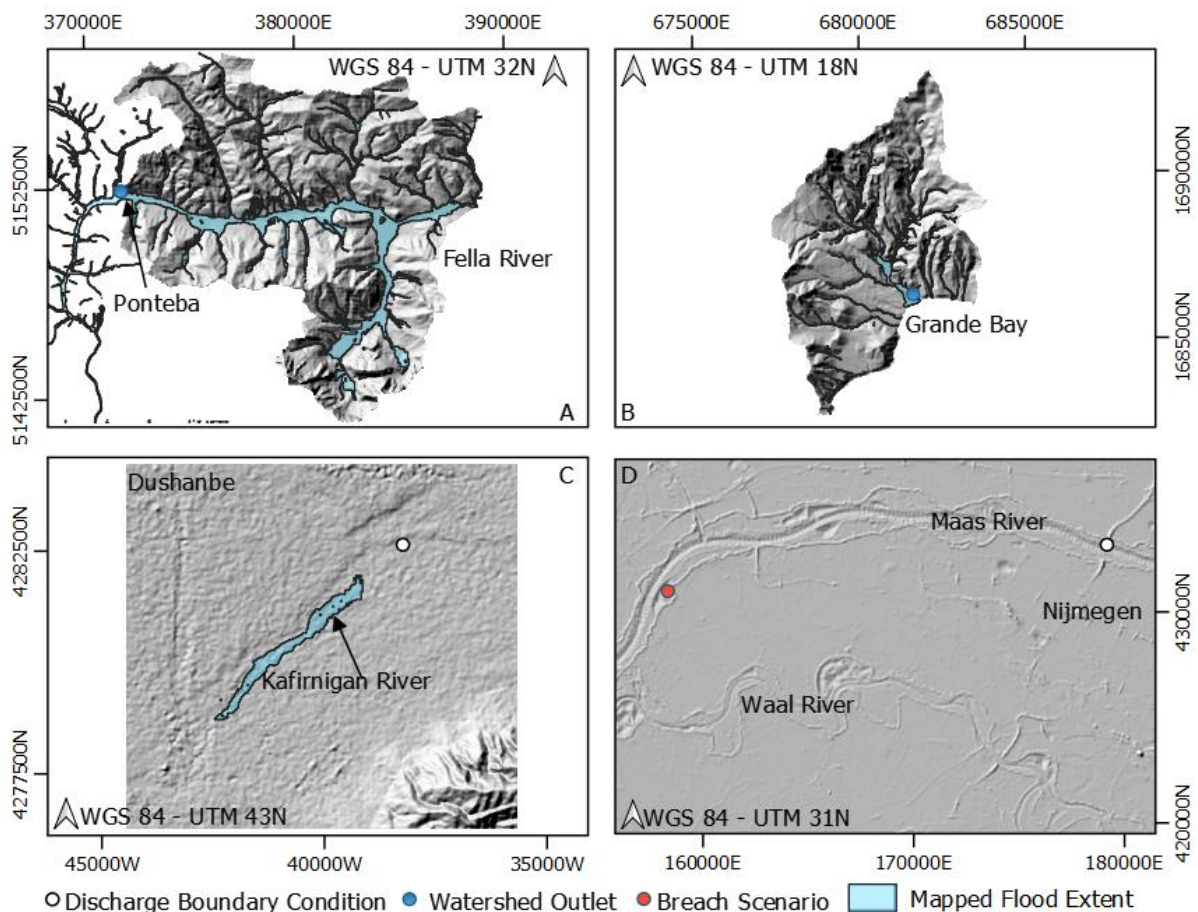
225 In this article, we verify the applicability and accuracy of the developed model on a set of three
226 study-sites and events. These events have been chosen to represent some of the various types of
227 context surrounding flood events.

228 The first study site is a watershed located on the South-East of the Caribbean island Dominica. Here,
229 around the town of Grande-Bay, Category-5 hurricane Maria made landfall in autumn 2017. With
230 over 500 mm of rainfall in 24 hours, flash floods destroyed vast parts of the island. The selected
231 catchment is described by Lidar-based elevation data (resampled to 10 meters), Mannings surface
232 roughness derived from field observations, the USGS field manual and a sentinel-2 based land use
233 map. Rainfall data is available from Canefield airport. For a further description of the area and event,
234 see also (Briones, 2019; Van Den Bout & Jetten, 2020)

235 The second event is a part of the Fella River basin, located in the Italian alps, with Ponteba chosen as
236 the outlet. On August 29, 2003, an intense cloud-burst resulted in major flashfloods throughout the
237 Fella basin, destroying houses and infrastructure throughout the steep valleys. Here again, mapped
238 flood extent is available, in combination with LIDAR elevation data, resampled to 20 meters
239 resolution. Additionally, land use and infiltration behavior was studied by . For a further description
240 of the area and event, see also (Borga, Boscolo, Zanoni, & Sangati, 2007; Bout & Jetten, 2018)

241 The third site is a river-segment located in central Tajikistan, just South of the capital Dushanbe. In
 242 this area, a 2016 precipitation event resulted in flooding along the Kafimigan river, just south of the
 243 capital Dushanbe. Here, 30-meter global SRTM elevation was filtered for high-frequency noise to
 244 improve quality of the terrain data. Mapped flood extents are available for a section of the river.
 245 Incoming discharge is provided as a boundary conditions on the upstream side of the river. We
 246 employ the discharge records for this area. The relevant return period discharge is provided as a
 247 boundary condition for both the presented SFFS method and the full dynamic simulation. For more
 248 information on the event and its impact, see also (van Westen, 2019)

249 The fourth and final study site is a segment of the River Maas, located in the central parts of the
 250 Netherlands. In this particular area, a circular levee-system (dijkkring 41), protects a sub-sealevel
 251 region of land from water in the Maas and Waal river. High-resolution fully dynamic modelling has
 252 been carried out for various levee breaching scenario's. Here, we utilize one of these scenarios as a
 253 reference for our developed method. We employ a boundary condition on the eastern side of the
 254 Maas, based on the assumptions from the scenarios in the national flood defense program of the
 255 Netherlands (Alkema & Middelkoop, 2005).



256

257 *Figure 3 Hillshaded elevation data for the study sites; A) Fella river basin in Northern Italy, B) Grande-Bay catchment in South-East Dominica, C) Kafirnigan River just South of Dushanbe, D) Levee ring 41, between the Maas and Waal rivers in the Netherlands.*

260 2.8 Hydrology and Calibration method

261 Hydrology was simulated identically for both the SFFS method and the full simulations. In the case of
 262 Grande-Bay and Fella, we employ a fixed infiltration percentage based on literature sources on the
 263 event. By making this choice, we attempt to provide a fair comparison of the methods, as both can

264 be linked to various more detailed hydrological systems that are beyond the scope of this work. For
 265 both the Dushanbe and Maas events, we assume infiltration and evapotranspiration during the event
 266 might be ignored. Calibration was carried out for both the presented method and the full dynamic
 267 flow simulations. A brute-force calibration approach was applied to the commonly chosen
 268 parameters. In this case, 6 parameter values were chosen on regular intervals between 50 and 150%
 269 of original values. The presented method was calibrated on 3 parameters: event duration, event net
 270 precipitation (infiltration is already subtracted), and Mannings Surface roughness coefficient. The full
 271 dynamical simulation was calibrated on 2 parameters: Mannings Surface roughness coefficient and
 272 infiltration percentage.

273 3. Results

274 3.1 Application, Accuracy and Speed

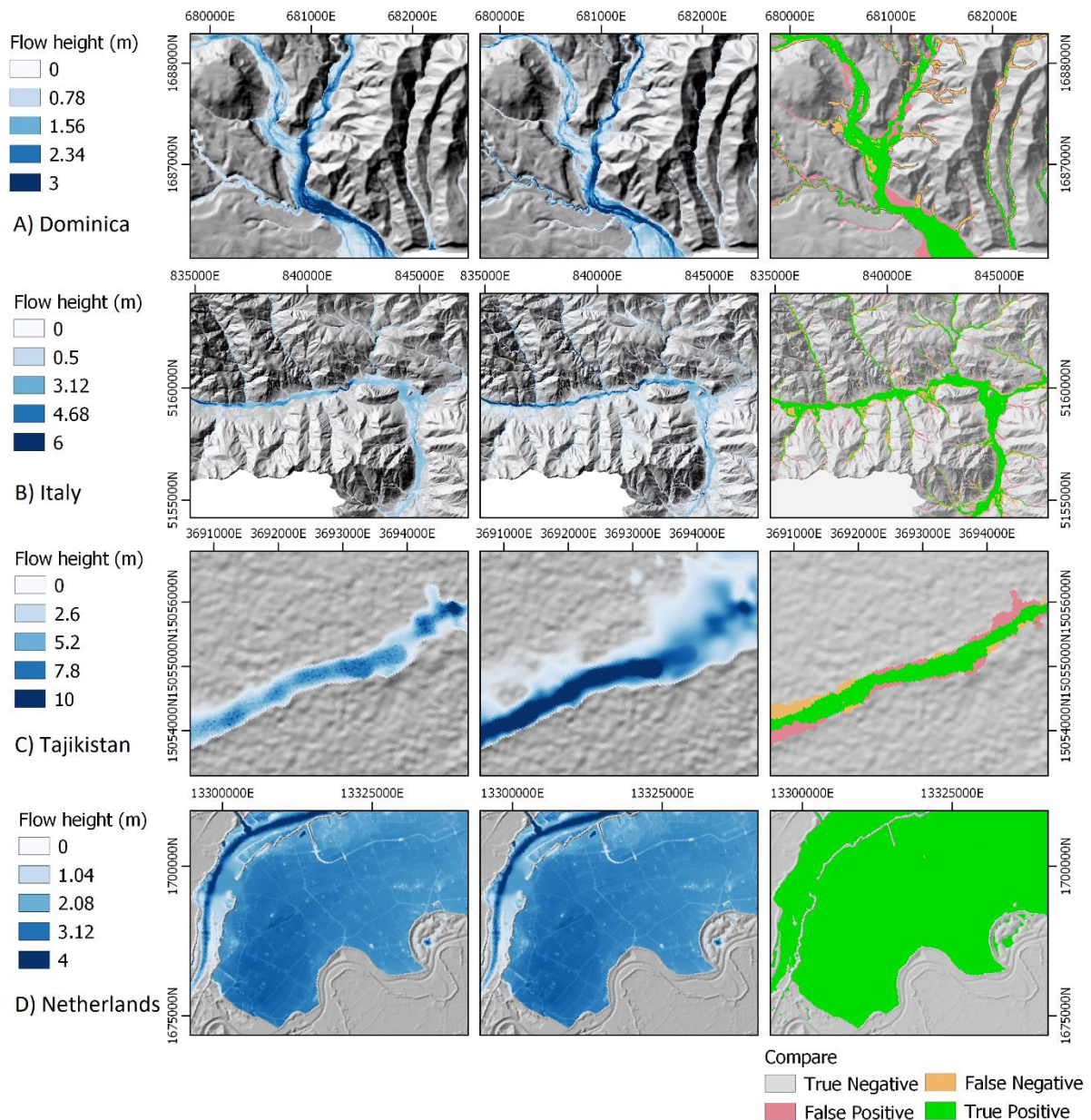
275 Below, we show a comparison with full dynamic simulations and mapped flood extent for various
 276 flood events in different environmental settings around the world (Italy, Dominica, Tajikistan and the
 277 Netherlands). These events were chosen to cover a range of flood types (flash floods, riverine
 278 flooding, levee systems), data quality contexts (high-resolution lidar data at 10 meters resolution or
 279 global SRTM elevation at 30 meters resolution), and domain sizes (between 34 and 617 km²). See the
 280 methodology and data section for a description of these areas, and the studied events.

281

282 *Table 1 Accuracy and computation time results for both the presented SFFS method, and full dynamic simulation. Accuracy is*
 283 *shown as percentage of correctly labeled pixels: flood or no flood.*

% Accuracy	UC Full (%)	CAL Full (%)	UC SFFS (%)	CAL SFFS (%)	Area (km ²)	Grid cell size (m)	CT – Full (seconds)*	CT -SFFS (seconds)*	Sens – Full (%)**	Sens – SFFS (%)**
Italy	92.10	92.26	93.8	94.95	180	20	2.2	2901	12.3	11.2
Dominica	95.34	95.69	94.52	95.54	34.7	10	1.3	1178	6.3	8.4
Tajikistan	86.78	87.08	96.87	98.23	71.7	30	0.42	195	-	-
Netherlands	100	100	99.13	99.91	875	40	2.1	880	-	-
St. Lucia	-	-	-	-	617	10	47	29940	-	-

284 UC = Uncalibrated, CAL = Calibrated, Full = full dynamic simulation, SFFS = Super-Fast-Flood-Simulation, CT = Compute Time
 285 *Average run-time per single simulation on AMD Threadripper 3970x, ** Sensitivity pertains to the average relative change
 286 in flood area compared to a relative change in input parameter

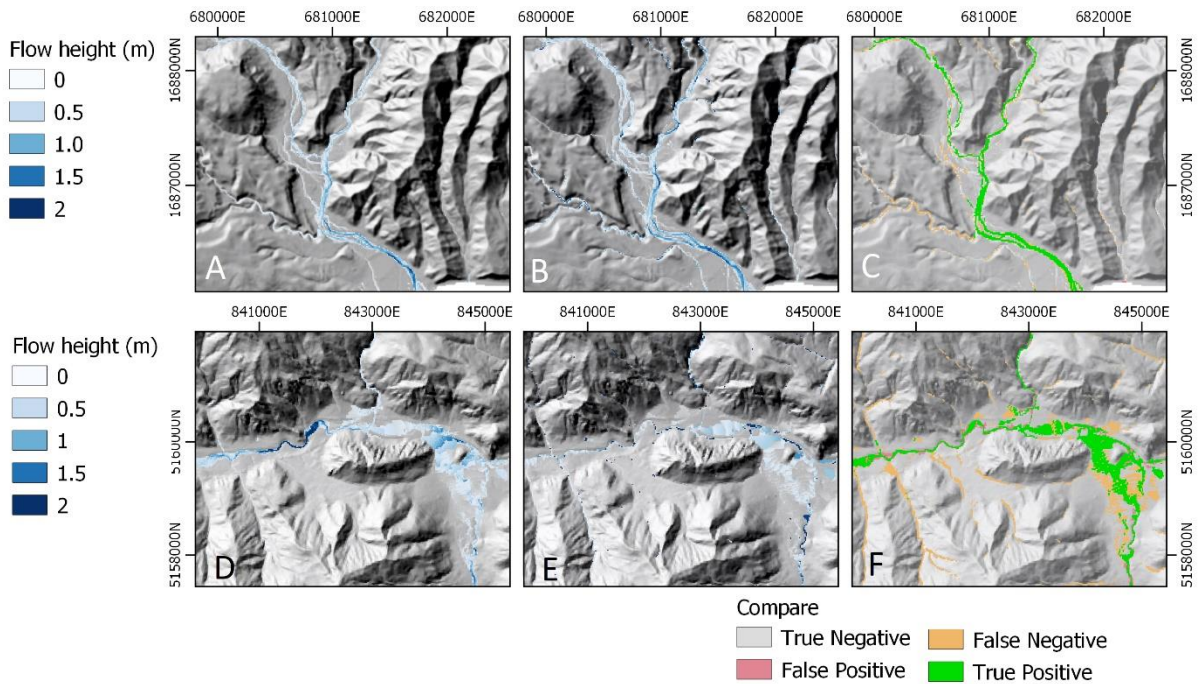


287

288 *Figure 4 Left) Maximum flow height for the presented SFFS method. Middle) Maximum flow height for full dynamic*
 289 *simulation. Right) Comparison of SFFS results and the observed flood extent. For the Maas flood (bottom), comparison is*
 290 *with reference high-resolution numerical simulation.*

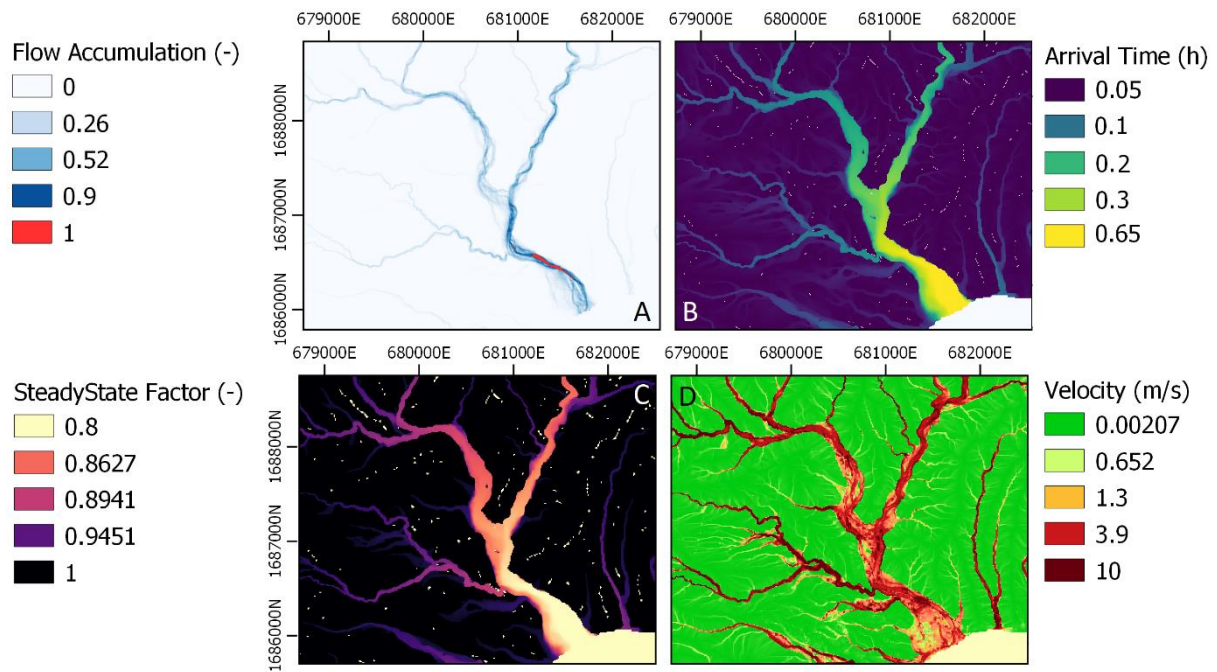
291 Over-all, the presented method is able to perform with an accuracy of 75.1%, as compared to an
 292 average accuracy of 93.8% for the full simulations. The performance is roughly equal in those cases
 293 with good elevation, whereas the results are worse for the case in Tajikistan, where a low quality
 294 SRTM DEM was used. Computation time was, on average, reduced by two orders of magnitude (avg.
 295 1514.5x). Despite the similarities in accuracy for the super-fast flood simulation and full dynamic flow
 296 simulation, there are aspects where the methods differ considerably. In many cases, elevation data
 297 contains hydrologically inconsistencies known as local depressions, often due to elevation model
 298 errors. Flood simulations suffer from these, as they influence total outflow and peak flow rates (Bout
 299 & Jetten, 2018). The narrow streams feeding the fella river (Figure 4C, Italy study case) are poorly
 300 captured in the elevation data, and water is effectively captured. Our method solves this problem by
 301 automatically considering a hydrologically corrected dem when specified by the user.

302 The simulated events all feature highly extreme occurrences of precipitation or discharge. To verify
 303 behavior of the model in the context of small precipitation events, the calibrated models are
 304 validated on events with 10 times reduced precipitation input. Here, reference flow extents are not
 305 available, but reference simulations using full dynamic models are used instead.



306
 307 *Figure 5 A comparison of the presented SFFS method and full dynamical simulation for a smaller event (1/10th the size of the*
 308 *event described earlier) for ABC) Dominica and DEF) Italy. A/D) SFFS maximum flow height results. B/E) Full simulation*
 309 *maximum flow height results. C/F) Comparison between SFFS and full dynamic simulation flood impact area.*

310 Besides the most commonly used hazard information (peak flow height and peak flow velocity),
 311 other information can be extracted from the model, such as flood arrival time, compensation factor
 312 for partial steady-state, b-coefficient, velocity field and the flow accumulation. For a more detailed
 313 explanation of these variables, please refer to the methods section.

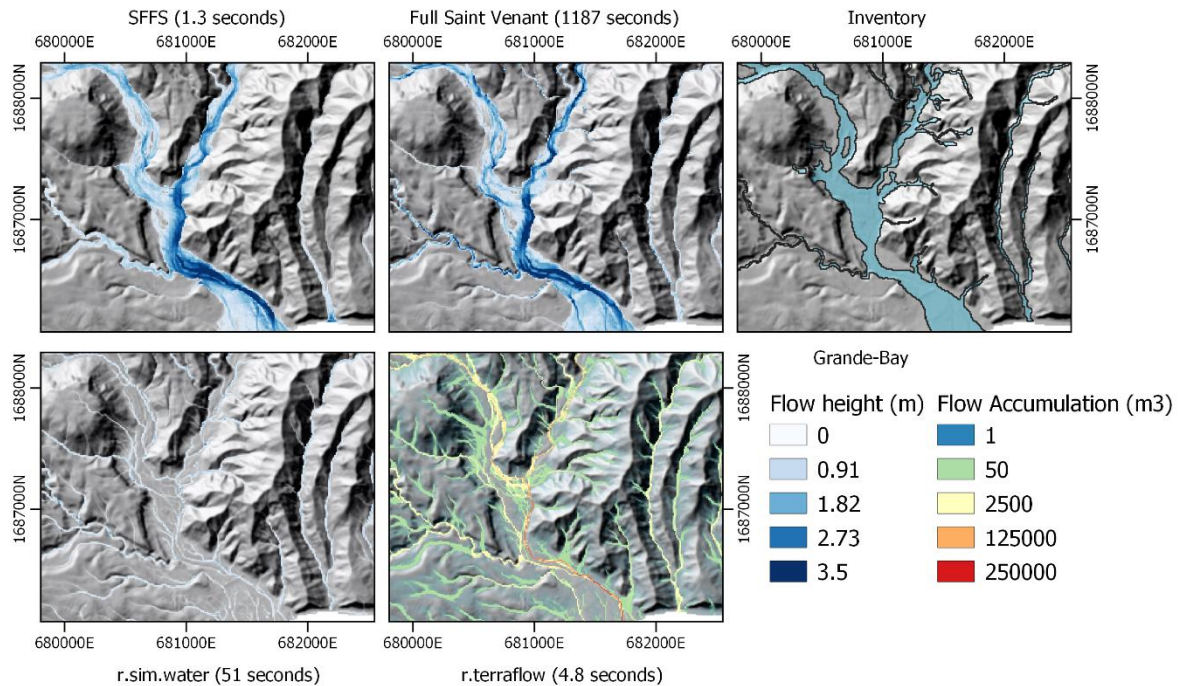


314

315 *Figure 6 Additional outcomes obtained from the presented SFFS method for Grande-Bay on Dominica. A) Flow accumulation,*
 316 *which in the steady-state assumption equals discharge. B) Flood arrival time, C) Compensation factor for the partial steady-*
 317 *state of the event. See the methodology for further details on this. D) Velocity during peak flow.*

318 3.2 Comparative Analysis

319 We compare our method with full dynamic Saint-Venant simulation, as well as popular methods for
 320 rapid flood hazard mapping: r.sim.water and r.terraflow. R.sim.water uses a stochastic particle-grid
 321 hybrid approach to map flow heights for a specified precipitation input. R.terraflow uses flow
 322 accumulation in multiple directions to estimate steady-state discharge.



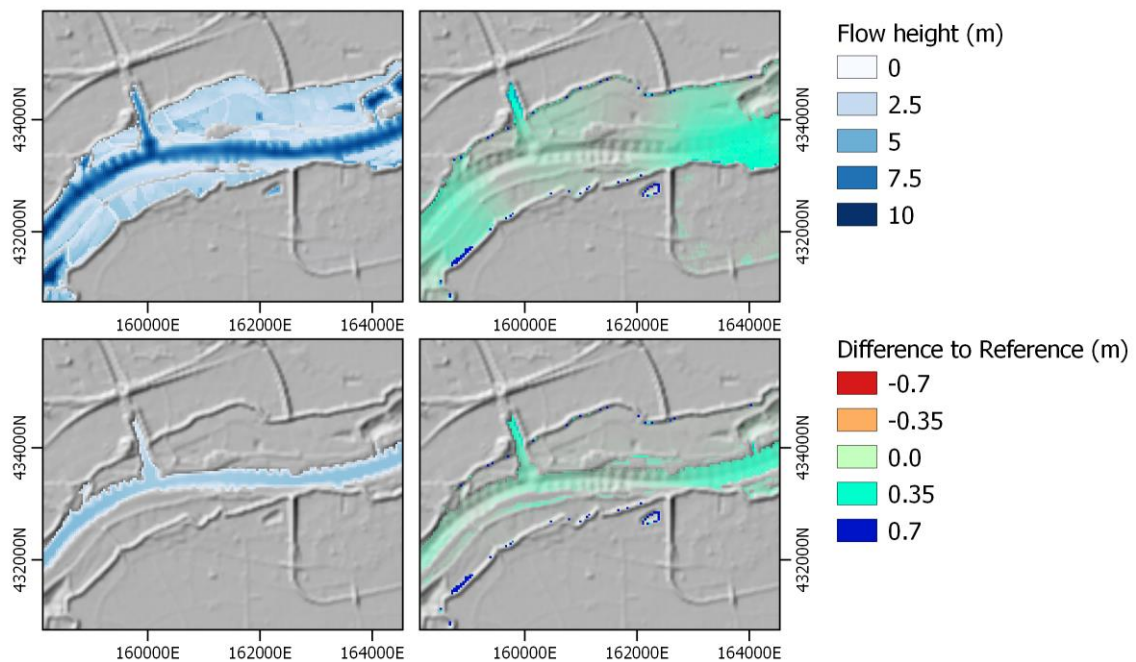
323

324 *Figure 7 Comparison of the presented method with full dynamics simulation, mapped flood extent (inventory), r.sim.water,*
 325 *and r.terraflow.*

326 The results of the comparison (figure 7), show that our presented method correctly implements
 327 water dynamics, including pressure-driven flow paths. Both r.sim.water and r.terraflow are limited by
 328 their flow paths, and show significantly longer computation time.

329 Other methods in the literature that focus on fast flood simulation show distinct limitations
 330 compared to the SFFS method. Cellular automata can be leveraged for fast approximate flood height
 331 maps, and show a reduction in simulation time between 250 and 1100 times (Jamali et al., 2019).
 332 However, these methods are only partially based on physical principles, and require additional
 333 empirical constants to be calibrated. Because if this, they cannot be used as easily in alternative
 334 scenario's where physical parameters of the landscape change. Additionally, cellular automata have
 335 not been applied to flash floods and riverine flooding, and have not been shown to work well with
 336 precipitation as a water source. Machine-learning based methods have similarly shown potential for
 337 fast flood simulation by learning networks based on full simulation results (Kabir et al., 2020).
 338 Currently, extensive training on large datasets of fully-simulated scenarios is required. After training,
 339 these methods show a reduction of simulation time similar to our method, but do not show the
 340 general applicability (Chu, Wu, Wang, Nathan, & Wei, 2020). These methods can not automatically
 341 adapt to new scenarios (e.g. implementation of levee-system, altered land use or application in
 342 another river-system). Such changes require expensive retraining of the neural networks.

343 In application to river systems, the method shows high accuracy in predicting spatial water heights in
 344 channel topography. For both high and low discharge in the Waal river, the new method predicts
 345 flow heights with a total flow height deviation of 4.6% for the high flow scenario and 4.3 percent for
 346 the low flow scenario (Figure 8).



347

348 *Figure 8 Comparison of simulated flow heights in the Waal river in the Netherlands for high discharge (top, 1200 m³/s) and*
 349 *low discharge (bottom, 240 m³/s)*

350 3.3 Discussion

351 The OpenLISEM SFFS model is based on various assumptions that require thorough consideration in
 352 case of application, such as the invertibility of flow accumulation to flow heights. Despite these
 353 assumptions, the over-all performance of the method is excellent compared to a state-of-the-art
 354 implementation of full dynamic flow simulation. In particular in consideration of the computation
 355 time, which was on average decreased by a factor 1514. The results of the simulation are limited as a
 356 SFFS method does not produce full dynamic output. However, the balance between quality, flexibility
 357 and compute time can be expected to benefit several common use-cases. The provided output (e.g.
 358 peak flow height, peak flow velocity, flood arrival time), are sufficient for a large portion of flood
 359 hazard studies. In hazard and risk assessment, estimation of annual risk is often directly carried out
 360 using peak flow heights, peak flow velocities, and vulnerability functions. It does remain important to
 361 note that the aim of the SFFS method is not to provide the most accurate flood hazard prediction.
 362 However, as long as the validity of the underlying assumptions are met, such as for our case studies,
 363 the application to risk reduction planning or early warning can be considered.

364 The computational time of the methods on consumer-level pc-hardware is an indication of new
 365 potential for flood hazard decision making. For areas smaller than 50km² at 10 meters resolution,
 366 computational times are smaller than 10 seconds even on common laptops. This is fast enough that a
 367 web-platform or application could provide some interactivity to users, with fast feedback on the
 368 effect of certain risk reduction alternatives in flood characteristics, allowing for fast iteration and
 369 efficient workflows. For many of the input parameters, there is no need to recalculate the entire
 370 simulation. Instead, near-instant results might be obtained in case of changes to surface roughness
 371 or event duration. Additionally, results from similarly-sized events can be used as preconditioning
 372 input for the model, and reduce compute time more. Further potential is visible in the field of early-
 373 warning systems. Running spatial rainfall input through flood simulations, taking into account
 374 ensembles of uncertain weather prediction, was a huge bottleneck but might now be possible (Bhola,

375 Leandro, & Disse, 2018). Finally, probabilistic flood hazard and risk assessment, often requiring
376 thousands of simulations, can be sped up to become practically applicable. Many alternative
377 scenario's including altered land cover, reservoirs, flow barriers and climate change can be simulated
378 in a fraction of the time.

379 4. Conclusions

380 Our SFFS model has the potential to alter the field of flood modelling. It shows two orders of
381 magnitude of increase in simulation speed, while obtaining highly similar accuracy as full dynamic
382 models in our presented case studies. With the reported increase in simulation speed, many avenues
383 of research and application might be unlocked, from ensemble modelling for uncertainty, user-
384 interactivity in web interfaces, or real-time modelling of large areas in early warning systems. Beyond
385 that, the presented method still shows several points of potential improvement that the wider flood
386 community might use to yield further improvements, such as the influence of water arrival time on
387 peak flows.

388 5. Data and Code availability

389 The data and code for the presented methods has been made publicly available under a GLP-3
390 license as part of the LISEM project.

391

392

393

394

395

6. References

- 396 Alkema, D., & Middelkoop, H. (2005). The influence of floodplain compartmentalization on flood risk
397 within the Rhine–Meuse Delta. *Natural hazards*, 36(1-2), 125-145.
- 398 Bhola, P. K., Leandro, J., & Disse, M. (2018). Framework for offline flood inundation forecasts for two-
399 dimensional hydrodynamic models. *Geosciences*, 8(9), 346.
- 400 Borga, M., Boscolo, P., Zanon, F., & Sangati, M. (2007). Hydrometeorological analysis of the 29
401 August 2003 flash flood in the Eastern Italian Alps. *Journal of hydrometeorology*, 8(5), 1049-
402 1067.
- 403 Bout, B., & Jetten, V. (2018). The validity of flow approximations when simulating catchment-
404 integrated flash floods. *Journal of hydrology*, 556, 674-688.
- 405 Briones, F. (2019). The endless hurricane: documenting life in the shelters, after Maria hit Dominica.
406 *Disaster Prevention and Management: An International Journal*.
- 407 Chu, H., Wu, W., Wang, Q., Nathan, R., & Wei, J. (2020). An ANN-based emulation modelling
408 framework for flood inundation modelling: Application, challenges and future directions.
409 *Environmental modelling & software*, 124, 104587.
- 410 de Saint-Venant, B. (1871). Theory of unsteady water flow, with application to river floods and to
411 propagation of tides in river channels. *French Academy of Science*, 73, 148-154.
- 412 Delestre, O., Cordier, S., Darboux, F., Du, M., James, F., Laguerre, C., . . . Planchon, O. (2014).
413 FullSWOF: A software for overland flow simulation. In *Advances in hydroinformatics* (pp. 221-
414 231): Springer.
- 415 Gibson, M. J., Savic, D. A., Djordjevic, S., Chen, A. S., Fraser, S., & Watson, T. (2016). Accuracy and
416 computational efficiency of 2D urban surface flood modelling based on cellular automata.
417 *Procedia engineering*, 154, 801-810.
- 418 Jamali, B., Bach, P. M., Cunningham, L., & Deletic, A. (2019). A Cellular Automata fast flood evaluation
419 (CA-ffé) model. *Water resources research*, 55(6), 4936-4953.
- 420 Kabir, S., Patidar, S., Xia, X., Liang, Q., Neal, J., & Pender, G. (2020). A deep convolutional neural
421 network model for rapid prediction of fluvial flood inundation. *Journal of hydrology*, 590,
422 125481.
- 423 Kalyanapu, A. J., Shankar, S., Pardyjak, E. R., Judi, D. R., & Burian, S. J. (2011). Assessment of GPU
424 computational enhancement to a 2D flood model. *Environmental modelling & software*,
425 26(8), 1009-1016.
- 426 Liang, Q., Du, G., Hall, J. W., & Borthwick, A. G. (2008). Flood inundation modeling with an adaptive
427 quadtree grid shallow water equation solver. *Journal of Hydraulic Engineering*, 134(11),
428 1603-1610.
- 429 Miller, J. E. (1984). *Basic concepts of kinematic-wave models* (2330-7102). Retrieved from
- 430 Mosavi, A., Ozturk, P., & Chau, K.-w. (2018). Flood prediction using machine learning models:
431 Literature review. *Water*, 10(11), 1536.
- 432 Rahman, A., Haddad, K., Zaman, M., Kuczera, G., & Weinmann, P. (2011). Design flood estimation in
433 ungauged catchments: a comparison between the probabilistic rational method and quantile
434 regression technique for NSW. *Australasian Journal of Water Resources*, 14(2), 127-139.
- 435 Sanders, B. F. (2017). Hydrodynamic modeling of urban flood flows and disaster risk reduction. In
436 *Oxford research encyclopedia of natural hazard science*.
- 437 Stelling, G. S., & Verwey, A. (2006). Numerical flood simulation. *Encyclopedia of hydrological sciences*.
- 438 Te Chow, V., Maidment, D., & Mays, L. (1962). Applied hydrology. *Journal of Engineering Education*,
439 308, 1959.
- 440 Van Den Bout, B., & Jetten, V. (2020). Catchment-scale multi-process modeling with local time
441 stepping. *Environmental earth sciences*, 79(8), 1-15.
- 442 van Westen, C. (2019). Procedure for the development of multi-hazard risk profiles at the district
443 level in Tajikistan.

- 444 Yu, D., & Lane, S. N. (2006). Urban fluvial flood modelling using a two-dimensional diffusion-wave
445 treatment, part 2: development of a sub-grid-scale treatment. *Hydrological Processes: An*
446 *International Journal*, 20(7), 1567-1583.
- 447 Zhao, H. (2005). A fast sweeping method for eikonal equations. *Mathematics of computation*, 74(250),
448 603-627.